

Article

The Co-Processing Combustion Characteristics of Municipal Sludge within an Industrial Cement Decomposition Furnace via Computational Fluid Dynamics

Ling Zhu , Ya Mao, Kang Liu, Chengguang Tong, Quan Liu and Qiang Xie * 

School of Mechanical and Electronic Engineering, Wuhan University of Technology, Luoshi Road, Wuhan 430070, China; 318728@whut.edu.cn (L.Z.); maoya@whut.edu.cn (Y.M.); 318648@whut.edu.cn (K.L.); 250132@whut.edu.cn (C.T.); quan_liu123@whut.edu.cn (Q.L.)

* Correspondence: q.xie@whut.edu.cn

Abstract: Dealing with municipal sludge in an effective way is crucial for urban development and environmental protection. Co-processing the sludge by burning it in a decomposition furnace in the cement production line has been found to be a viable solution. This work aims to analyze the effects of the co-disposal of municipal sludge on the decomposition reactions and NO_x emissions in the decomposing furnaces. Specifically, a practical 6000 t/d decomposition furnace was taken as the research object. To achieve this, ANSYS FLUENT with a UDF (user-defined function) was applied to establish a numerical model coupling the limestone decomposition reaction, fuel combustion, and NO_x generation and reduction reactions. The flow, temperature, and component field distributions within the furnace with no sludge were firstly simulated with this model. Compared with site test results, the model was validated. Then, with sludge involved, the structure and operation parameters of the decomposition furnace for the co-disposal of municipal sludge were investigated by simulating the flow field, temperature field, and component field distributions. Parametric studies were carried out in three perspectives, i.e., sludge mixing ratio, preheating furnace arrangement height, and sludge particle size. The results show that all three aspects have great importance in the decomposing process. A set of preferable values, including a sludge mixing ratio of 10%, preheating furnace height of 21.5 m, and sludge particle diameter of 1.0 mm, was obtained, which resulted in a raw material decomposition rate of 89.9% and a NO volume fraction of 251 ppm at the furnace outlet.

Keywords: municipal sludge; combustion process; decomposition furnace; cement production line; collaborative disposal; computational fluid dynamics

MSC: 80A25; 76-10; 76F80



Citation: Zhu, L.; Mao, Y.; Liu, K.; Tong, C.; Liu, Q.; Xie, Q. The Co-Processing Combustion Characteristics of Municipal Sludge within an Industrial Cement Decomposition Furnace via Computational Fluid Dynamics. *Mathematics* **2024**, *12*, 147. <https://doi.org/10.3390/math12010147>

Academic Editors: Roman Ivanovich Parovik and Aleksander Kartushinsky

Received: 18 November 2023

Revised: 20 December 2023

Accepted: 30 December 2023

Published: 2 January 2024



Copyright: © 2024 by the authors. Licensee MDPI, Basel, Switzerland. This article is an open access article distributed under the terms and conditions of the Creative Commons Attribution (CC BY) license (<https://creativecommons.org/licenses/by/4.0/>).

1. Introduction

The production of municipal sludge is on the rise globally due to population growth, industrialization, and urbanization [1]. For example in the European Union (EU), the sludge increased from approximately 11.8 million dry tons in 2010 to 13 million dry tons in 2020 even after the implementation of related legislation [2]. Effective sludge processing has become a global priority. Taking China as an example, the Chinese “14th Five-Year Plan” for the Development of municipal Sewage Treatment and Resource Utilization clearly states that the rate of harmless disposal of municipal sludge should reach over 90% by 2025, and the harmless disposal of sludge should be fully realized by 2035. In order to reduce the impact of sewage sludge on the environment as well as life, the reasonable disposal of municipal sewage sludge has become an environmental problem that people urgently need to solve [3]. Conventional sludge disposal methods such as landfill, composting, and ocean dumping are constrained by environmental protection policies, making sludge incineration a more viable disposal option [4].

The utilization of decomposition furnaces for the disposal of municipal sludge is a viable practice in the industry. These furnaces play a vital role in achieving the pre-decomposition of raw materials within cement production [5]. Its internal temperature can ensure the complete decomposition of organic matter contained in sludge. In addition, the heat value of the organic matter could be utilized. Additionally, the ash residue after the combustion of the inorganic components can be used as raw material for the production of cement clinker. Harmful heavy metals in the ash will be incorporated into the clinker minerals, without adversely affecting the quality of the cement. Due to these advantages, the co-processing technology of municipal sludge in cement decomposition furnaces will probably be commonly employed in the future.

There are complex flows, combustion, and heat and mass transfer, as well as chemical reaction processes, inside a cement decomposition furnace. Consequently, these issues have received significant attention, leading to numerous investigations. Valdes [6] found that mixing sewage sludge with other fuels allowed for both constant combustion of the original fuel and disposal of the sewage sludge. Magdziarz [7] used mass spectrometry–thermogravimetry to study the combustion process of sludge with different chemical compositions, obtaining pyrolysis curves that, although with different values, were similar to the combustion of pulverized coal in terms of combustion processes and phases. Li et al. [8] investigated the effect of the combustion of dry and hydrothermal sludge on CaCO_3 decomposition, and the results showed that hydrothermal sludge combustion may produce less NO , and also obtained the best methodology model for fitting the CaCO_3 composition phase. He [9] studied the effect of sludge addition on the water resistance of cement during mixing and found that the appropriate sludge mixing ratio does not affect the cement quality. Wang et al. [10] conducted thermogravimetric analysis of the combustion process of a mixture of sludge and straw in air, and the results showed that the mixing of the two had a promotional effect on their respective combustion. Fang et al. [11] and Lv et al. [12] found, respectively, in their experiments that the reducing components such as HCN , NH_3 , and alkanes released from the sludge during the mixed combustion contributed to the reduction of NO in the decomposition furnace. Fang et al. [13] further investigated the effects of sludge dosage, oxygen concentration, and other factors on NO concentration in cement industry flue gas in a fluidized bed reactor and determined the optimal operating conditions for the sludge denitrification process.

There are many researchers applying CFD (computational fluid dynamics) techniques to numerically simulate the multiphase flow, combustion, and raw material decomposition processes in the decomposition furnace. Nakhaei [14] investigated the gas–solid flow in a decomposition furnace using the Eulerian–Lagrangian approach together with the multiphase particle-in-cell method. The accuracy of the Gidaspow drag model and the EMMS (energy-minimization multi-scale) model was compared by studying the particle dispersion and temperature distribution in different regions of the decomposition furnace. Mikulčić et al. [15,16] treated the raw material decomposition reaction with the fuel combustion reaction by using the Eulerian–Lagrangian method and analyzed the co-firing of biomass replacing 10%, 20%, and 30% of coal. The results showed that special attention needs to be paid to the complete oxidation of char particles to avoid undesired instabilities in the preheating system. M. Zeneli [17] defined the gas phase as the fluid Eulerian phase and sorbent particles and coal particles as two granular phases. The Eulerian–Eulerian method was used to simulate the gas–solid flow in the decomposition furnace. Wang et al. [18] took the Trinal-sprayed decomposition furnace as the research object and applied CFD technology to simulate the effect of coal and sludge mixed combustion. The results showed that the temperature was reduced and the decomposition rate decreased after adding sludge. Hu [19] used CFD techniques to research a furnace with coal and sludge mixing. Parameters such as sludge mixing ratio, sludge moisture content, and secondary air distribution were optimized.

However, there are still some shortcomings for these previous studies. Firstly, in some investigations [14–17], only one of the Eulerian–Eulerian or Eulerian–Lagrangian

methods has been used for simulation, without addressing the coupling of the raw material decomposition reaction with the fuel combustion reaction. Secondly, when studying the coal–sludge blending combustion, some studies [18,19] directly inject coal and sludge from the same inlet. This makes the sludge with higher water content have a greater impact on the temperature of the main region where the raw meal decomposition reaction occurs in the decomposition furnace, which in turn affects the raw meal decomposition rate.

Aiming at these problems, here, in this work, raw material decomposition reaction is incorporated into the model using the Eulerian–Eulerian method while the fuel combustion reaction is coupled into the model using the Eulerian–Lagrangian method. Meanwhile, other suitable numerical models such as the turbulence model and radiation model are applied to analyze the decomposition furnace. The model is verified based on data obtained from the field experimental measurements. Then, a sludge preheating furnace is arranged to allow the sludge to enter the decomposition furnace from the preheating furnace. Finally, the preheating furnace and the decomposition furnace are numerically simulated as a whole body. The combustion and co-processing inside are analyzed from three aspects, namely the sludge mixing ratio, preheating furnace arrangement height, and sludge size.

The rest of the paper is organized as follows. Section 2 describes the model applied in this work with geometry details (Section 2.1), theoretical equations (Section 2.2), and simulation conditions (Section 2.3) included. Section 3 gives the simulated results and related discussions. Analysis between combustion without (Section 3.1) and with (Section 3.2) sludge involved were compared. Section 4 draws the main conclusions in this work.

2. Model Description

2.1. Geometry Model

Figure 1 gives the full-scale geometry model of an industrial 6000 d/t decomposition furnace system, which has a height of 64 m. As illustrated, the kiln flue gas inlet diameter d_1 is 2800 mm. The flue gas exhausting from the kiln end flue chamber flows through the mouth of the decomposition furnace into the cone body. Two groups of four fuel inlets in total are installed at the top of the cone body of the furnace. The two groups are arranged at an interval of 180° . Each group has a vertical spacing of 1000 mm for the upper and lower inlets. Each inlet has a diameter d_5 of 300 mm and an angle of 30° to the central axis of the furnace. The tertiary air inlet is eccentric, with a distance of 1500 mm from the center axis of the furnace and a cross-sectional dimension of 2200×2800 mm. Gradient combustion technology is applied for raw materials on the decomposing furnace. The raw material inlets 1 and 2 are located at a height of 21.2 m, while the inlets 3 and 4 are positioned at 11.2 m. All four inlets have a diameter of 800 mm and lie at an angle of 60° to the horizontal plane. The preheating furnace features a sludge inlet diameter of 900 mm and a hot air inlet diameter of 1500 mm. Other details can be found in the schematic diagram and Table 1.

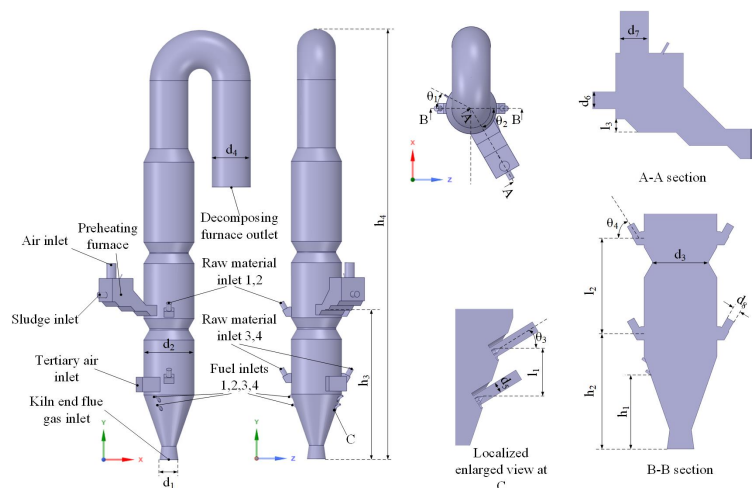


Figure 1. Geometric modeling of decomposition furnace system.

Table 1. Dimensional parameters of the decomposition furnace system.

Parameter	Value	Unit
Kiln end flue gas inlet diameter, d_1	2800	mm
Decomposition furnace column combustion chamber diameter, d_2	7600	mm
Decomposition furnace internal indentation diameter, d_3	5870	mm
Decomposition furnace outlet diameter, d_4	5800	mm
Inlet diameter of coal injection pipe, d_5	300	mm
Sludge inlet diameter, d_6	900	mm
Preheating furnace air inlet diameter, d_7	1500	mm
Raw material inlet diameter, d_8	800	mm
Vertical distance between upper and lower coal injection pipes, l_1	1000	mm
Vertical distance between upper and lower raw material discharging pipes, l_2	10,000	mm
Vertical distance between upper and lower grates, l_3	700	mm
Height of lower coal injection pipe, h_1	8000	mm
Height of lower raw material discharging pipes, h_2	11,200	mm
Height of preheating furnace arrangement position, h_3 (variable)	15.5–33.5	m
Decomposition furnace height, h_4	64,200	mm
Angle between coal injection pipe and raw material discharging pipes, θ_1	30	°
Angle between preheating furnace and raw material discharging pipes, θ_2	60	°
Angle between coal injection pipe and horizontal plane, θ_3	30	°
Angle between raw material discharging pipes and horizontal plane, θ_4	60	°

2.2. Governing Equations

2.2.1. Euler Multiphase Model

For the simulation of gas–solid two-phase flow, the Eulerian–Lagrangian and Eulerian–Eulerian methods are the two main CFD methods [20,21]. The Eulerian–Lagrangian method is able to calculate the trajectory of the solid phase with the mass, momentum, and energy exchanges that take place between the solid phase and the continuous phase during its motion. The Eulerian–Eulerian method simplifies the solid phase by introducing the concept of phase volume fraction α , treating the solid phase as a continuous medium and calculating its properties through kinetic theory. The Eulerian–Lagrangian model can be used when the solid phase volume fraction is low, while the Eulerian–Eulerian model should be used when the solid phase volume fraction is not negligible.

There are three Eulerian phases in the computational simulation of this work, which are the flue gas phase, the sorbent granular phase $CaCO_3$, and the product granular phase CaO . The pulverized coal particles, on the other hand, are represented using the Eulerian–Lagrangian method due to its low volume fraction.

In the Euler multiphase flow model, the mass conservation equations for the gas phase, the sorbent phase, and the product phase are, respectively, given by

$$\frac{\partial}{\partial t}(\alpha_g \rho_g) + \nabla \cdot (\alpha_g \rho_g \vec{u}_g) = \dot{m}_{sg} \quad (1)$$

$$\frac{\partial}{\partial t}(\alpha_s \rho_s) + \nabla \cdot (\alpha_s \rho_s \vec{u}_s) = -\dot{m}_{sg} - \dot{m}_{sp} \quad (2)$$

$$\frac{\partial}{\partial t}(\alpha_p \rho_p) + \nabla \cdot (\alpha_p \rho_p \vec{u}_p) = \dot{m}_{sp} \quad (3)$$

where subscripts g , s , and p represent the gas, sorbent, and product phase, respectively; ρ and u are, respectively, the density and velocity of each phase; \dot{m}_{sg} and \dot{m}_{sp} are the mass transmission from the sorbent phase to gas phase and the mass transmission from the sorbent phase to product phase, respectively.

The momentum conservation for the gas phase, the sorbent phase, and the product phase are, respectively, given by

$$\begin{aligned} \frac{\partial}{\partial t}(\alpha_g \rho_g \vec{u}_g) + \nabla \cdot (\alpha_g \rho_g \vec{u}_g \vec{u}_g) = & -\alpha_g \nabla P_g + \nabla \cdot \overline{\overline{\tau}}_q + \alpha_g \rho_g \vec{g} \\ & + K_{sg}(\vec{u}_s - \vec{u}_g) \\ & + K_{pg}(\vec{u}_p - \vec{u}_g) + \dot{m}_{sg} \vec{u}_s \end{aligned} \tag{4}$$

$$\begin{aligned} \frac{\partial}{\partial t}(\alpha_s \rho_s \vec{u}_s) + \nabla \cdot (\alpha_s \rho_s \vec{u}_s \vec{u}_s) = & -\alpha_s \nabla P_g - \nabla P_s + \nabla \cdot \overline{\overline{\tau}}_s + \alpha_s \rho_s \vec{g} \\ & + K_{gs}(\vec{u}_g - \vec{u}_s) \\ & + K_{ps}(\vec{u}_p - \vec{u}_s) - \dot{m}_{sg} \vec{u}_s - \dot{m}_{sp} \vec{u}_s \end{aligned} \tag{5}$$

$$\begin{aligned} \frac{\partial}{\partial t}(\alpha_p \rho_p \vec{u}_p) + \nabla \cdot (\alpha_p \rho_p \vec{u}_p \vec{u}_p) = & -\alpha_p \nabla P_g - \nabla P_p + \nabla \cdot \overline{\overline{\tau}}_p + \alpha_p \rho_p \vec{g} \\ & + K_{gp}(\vec{u}_g - \vec{u}_p) \\ & + K_{sp}(\vec{u}_s - \vec{u}_p) + \dot{m}_{sp} \vec{u}_s \end{aligned} \tag{6}$$

where K_{sg} is equal to K_{gs} , K_{ps} is equal to K_{sp} , K_{gp} is equal to K_{pg} , and the three are the momentum exchange coefficients between the phases. The stress tensor $\overline{\overline{\tau}}$ is given by

$$\overline{\overline{\tau}} = \alpha \mu (\nabla \vec{u} + \nabla \vec{u}^T) + \alpha \left(\lambda - \frac{2}{3} \mu \right) \nabla \cdot \vec{u} \vec{I} \tag{7}$$

where μ and λ are the shear and bulk viscosity; \vec{I} is the unit tensor.

The energy conservation equation for each phase i ($i = g, s, p$) is given by

$$\frac{\partial}{\partial t}(\alpha_i \rho_i h_i) + \nabla \cdot (\alpha_i \rho_i \vec{v}_i h_i) = \alpha_i \frac{\partial P_i}{\partial t} + \overline{\overline{\tau}}_i \cdot \nabla \vec{u}_i - \nabla \cdot \vec{q}_i + \sum_{j=1, j \neq i}^n \dot{Q}_{ji} + S_i \tag{8}$$

where h_i , S_i , \vec{q}_i , and \dot{Q}_{ji} are, respectively, the species enthalpy of phase i , the source term that includes sources of enthalpy due to homogeneous and heterogeneous chemical reaction or radiation, the heat flux of phase i , and the rate of energy transfer between phases.

2.2.2. Discrete Phase Model

The discrete phase model in Fluent follows the Eulerian–Lagrangian method [20]. The discrete phase model calculates the trajectory of coal particles by integrating the force balance on the particle. This force balance equates the particle inertia with the force acting on the particle and can be written as

$$m_p \frac{d\vec{u}_p}{dt} = m_p \frac{\vec{u}_g - \vec{u}_p}{\tau_r} + m_p \frac{\vec{g}(\rho_p - \rho_g)}{\rho_p} + \vec{F} \tag{9}$$

where m_p , u_g , u_p , ρ_g , ρ_p , and \vec{F} are, respectively, the particle mass, the gas phase velocity, the particle velocity, the gas phase density, the density of the particle, and the additional force. $m_p \frac{\vec{u}_g - \vec{u}_p}{\tau_r}$ is the drag force, and τ_r is the particle relaxation time calculated by

$$\tau_r = \frac{\rho_p d_p^2}{18 \mu_g C_d \text{Re}} \tag{10}$$

where μ_g and d_p are the gas dynamic viscosity and the particle diameter, respectively. Re is the relative Reynolds number, which is defined as

$$\text{Re} = \frac{\rho_g d_p |\vec{u}_p - \vec{u}|}{\mu_g} \tag{11}$$

2.2.3. Turbulence Model

For flows with refluxes and swirls, the standard $k - \epsilon$ model is considered to be the most suitable turbulence model due to its advantages in computation time and convergence.

Consequently the standard $k - \varepsilon$ model is employed as the gas-phase turbulence model. The turbulent kinetic energy k and the turbulent dissipation rate ε need to be solved [22], and they are given by:

$$\frac{\partial}{\partial t}(\rho k) + \frac{\partial}{\partial x_i}(\rho k u_i) = \frac{\partial}{\partial x_i} \left[\left(\mu + \frac{\mu_t}{\sigma_k} \right) \frac{\partial k}{\partial x_j} \right] + G_k + G_b - \rho \varepsilon \tag{12}$$

$$\frac{\partial}{\partial t}(\rho \varepsilon) + \frac{\partial}{\partial x_i}(\rho \varepsilon u_i) = \frac{\partial}{\partial x_i} \left[\left(\mu + \frac{\mu_t}{\sigma_\varepsilon} \right) \frac{\partial \varepsilon}{\partial x_j} \right] + C_{1\varepsilon} \frac{\varepsilon}{k} G_k - C_{2\varepsilon} \rho \frac{\varepsilon^2}{k} + S_\varepsilon \tag{13}$$

where G_k and G_b are, respectively, the turbulent kinetic energy from the velocity gradient and the turbulent kinetic energy from buoyancy. Other constants include $C_{1\varepsilon} = 1.44$, $C_{2\varepsilon} = 1.92$. $\sigma_k = 1.0$ and $\sigma_\varepsilon = 1.3$ are the turbulent Prandtl numbers for k and ε . The turbulent eddy viscosity μ_t is given by:

$$\mu_t = \rho C_\mu \frac{k^2}{\varepsilon} \tag{14}$$

where C_μ is a constant with the value 0.09.

2.2.4. Radiation Model

The albedo coefficient, optical thickness, and radiation-conduction parameters have an influence on the heat transfer behavior of the system [23,24]. Among the six radiation models provided by Fluent, only the $P1$ model and DO (discrete ordinate) model can be used to simulate the radiation between the solid phase and gas phase. The $P1$ model is mainly used when the optical thickness is greater than 1. The DO model is more appropriate for optically thin problems. Moreover, the DO model takes longer to compute than the $P1$ model. Consequently, the $P1$ model is applied in this work as the radiation model [25]. In the $P1$ model, the radiative heat flux q_r can be calculated by

$$q_r = -\frac{1}{3(a + \sigma_s) - C\sigma_s} \nabla G \tag{15}$$

where a and σ_s represent the absorption and scattering coefficients, respectively. G is the amount of incident radiation, and C is the linear anisotropic phase function coefficient. After introducing the parameter

$$\Gamma = \frac{1}{3(a + \sigma_s) - C\sigma_s} \tag{16}$$

Equation (15) simplifies into

$$q_r = -\Gamma \nabla G \tag{17}$$

The transport equation for G is given by

$$\nabla \cdot (\Gamma \nabla G) - aG + 4an^2\sigma T^4 = S_G \tag{18}$$

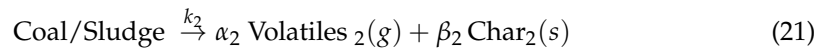
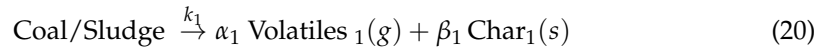
where n is the refractive index of the medium, σ is the Stefan-Boltzmann constant, and S_G is the user-defined radiation source. Combining Equations (17) and (18), the following equation can be obtained:

$$-\nabla \cdot q_r = aG - 4an^2\sigma T^4 \tag{19}$$

Equation (19) can be directly substituted into the energy equation to account for the heat source due to radiation. When the $P1$ model is used as the radiation model, the internal emissivity of the wall defaults to 0.5, while the emissivity of the flow inlets and outlets defaults to 1.0.

2.2.5. Combustion Model for the Coal and Sludge

Coal and municipal sludge will be rapidly heated and undergo a series of transformation processes when interacting with the furnace gases [26]. Therefore, a two-competing-rates model was employed to simulate the coal and sludge volatilization processes [27]. The model uses two first-order equations to control the reaction at low and high temperatures, which is described as



$$k_1 = A_1 \exp\left(\frac{E_1}{RT_p}\right) \tag{22}$$

$$k_2 = A_2 \exp\left(\frac{E_2}{RT_p}\right) \tag{23}$$

where k_1 and k_2 are the competitive volatilization rates at low and high temperatures, respectively. The kinetics/diffusion controlled reaction rate model was applied for modeling the coke combustion reaction [28,29]. The reaction rate is determined by the diffusion rate of the gaseous oxidant to the particle surface and the internal reaction kinetics, and the rate of coke combustion is given by

$$R_1 = C_1 \frac{[(T_p + T_\infty)/2]^{0.75}}{D_p} \tag{24}$$

$$R_2 = C_2 \exp\left(-\frac{E}{RT_p}\right) \tag{25}$$

where R_1 , C_1 , D_p , T_p , T_∞ , R_2 , C_2 , and E are, respectively, the diffusion rate, the diffusion rate constant, the diameter of coke, the temperature of coke, the temperature of atmosphere around coke, the kinetic rate, the pre-exponential factor, and the activation energy.

The diffusion rate and the chemical reaction rate are weighted in a certain ratio. When considered together, the reaction rate of coke is obtained by

$$\frac{d_{m_p}}{dt} = -\pi D_p^2 p \frac{\rho R T_\infty Y_{ox}}{M_{w,ox}} \frac{R_1 R_2}{R_1 + R_2} \tag{26}$$

where p is the partial pressure of the gas around the particles and Y_{ox} is the mass fraction of oxygen in the gas.

2.2.6. Species Transport Model

The species transport model is employed to solve the component transport process and its chemical reactions [30]. The generalized form of the conservation equation is described by

$$\frac{\partial}{\partial t}(\rho Y_i) + \nabla(\rho \vec{v} Y_i) = -\nabla \vec{J}_i + R_i + S_i \tag{27}$$

where Y_i , R_i , S_i , and \vec{J}_i are the mass fraction of substance i , the net production rate of the chemical reaction, the rate of additional production due to discrete phases and user-defined source terms, and the diffusive flux of substance i , respectively. Finite-rate/eddy dissipation was applied for the species transport modeling of the gas-phase combustion reaction in the furnace. The model calculates both the Arrhenius and eddy dissipation equations, combining kinetic and turbulence factors, with the following response equations:

$$R_r = A_r T^{\beta_r} \exp\left(-\frac{E}{RT}\right) \tag{28}$$

$$R_{i,r} = V'_{i,r} M_{w,i} A B \rho \frac{\varepsilon}{K} \frac{\sum_P Y_P}{\sum_j^N V''_{j,r} M_{w,j}} \tag{29}$$

where R_r , $R_{i,r}$, A_r , T^{β_r} , E , $V'_{i,r}$, $V''_{j,r}$, and $M_{w,j}$ are the chemical reaction rate of reaction r , the chemical reaction rate of component i in reaction r , the pre-exponential factor of reaction r , the temperature coefficient, the activation energy, the stoichiometric number of reactant i in reaction r , the stoichiometric number of product j in reaction r , and the molecular weight of the component j , respectively. The reaction rates are the minimum values of the calculation results between Equations (28) and (29).

2.2.7. Raw Material Decomposition Model

The chemical equation for the decomposition of raw material and the reaction rate are stated as



$$R = K \prod_{j=1}^{Nr} [C_j]^{st} \tag{31}$$

where Nr , C_j , and st are the total number of reactants, the molar concentration of the reactants, and the chemical equivalent stoichiometry coefficient of the reactants, respectively. K is the rate constant of the reaction, which is determined by the partial pressure of carbon dioxide [31–33], i.e., P_{CO_2} . It is described as

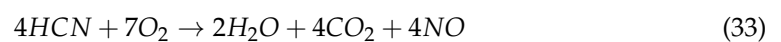
$$K = \begin{cases} A \exp\left(-\frac{E}{RT}\right) & P_{CO_2} < 10^{-2} P_{eCO_2} \\ A \exp\left(-\frac{E}{RT}\right) \frac{P_{eCO_2} - P_{CO_2}}{P_{eCO_2}} & 10^{-2} P_{eCO_2} < P_{CO_2} < P_{eCO_2} \\ 0 & \text{else} \end{cases} \tag{32}$$

where R , A , E , and P_{eCO_2} are the universal gas constant, the pre-exponential factor, the activation energy, and the equilibrium pressure of carbon dioxide, respectively. $E = 187.3$ kJ/mol and $A = 1.221 \times 10^9$ (s⁻¹) are obtained experimentally [34].

2.2.8. Modeling of NOx Generation and Reduction

Since the temperature inside a decomposition furnace is generally 800 °C–1200 °C, the thermal NOx and fast NOx generation is very small in this case. The NOx calculation only considers the fuel NOx generated by fuel combustion and NOx in the flue gas at the kiln end.

In this work, the fuel NOx generation mechanism model proposed by De’Soete [35] is applied to simulate the process of NO generation inside the decomposition furnace. The N element in the fuel is pyrolyzed with the C and H elements in the gas to generate the intermediate component HCN, and the oxidation of NO generation equations and reaction rates are given by

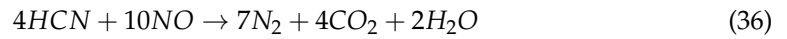


$$R_{HCN \rightarrow NO} = 10^{11} \rho_g Y_{HCN} (Y_{O_2})^b e^{-33,700/T_g} \tag{34}$$

where Y_i is the mass fraction of component i ; ρ_g is the density of the gas mixture; T_g is the temperature of the gas mixture; and the oxygen reaction level b is a segmented linear function of the oxygen concentration X_{O_2} .

$$b = \begin{cases} 1.0 & \ln X_{O_2} \leq -5.5 \\ 0.2 - 0.8(\ln X_{O_2} + 4.5) & -5.5 \leq \ln X_{O_2} \leq -4.5 \\ 0.071(-\ln X_{O_2} - 3.0) & -4.5 \leq \ln X_{O_2} \leq -3.0 \\ 0 & -3.0 < \ln X_{O_2} \end{cases} \quad (35)$$

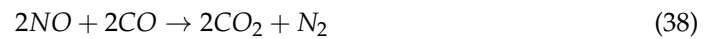
At the same time, the NO generated is reduced to N_2 by HCN with the reaction equation and rate described, respectively, by



$$R_{NO \rightarrow O_2} = 3 \times 10^{12} \rho_g Y_{HCN} Y_{NO} e^{-30,000/T_g} \quad (37)$$

Due to the incomplete combustion of coke, a reducing gas, with mainly CO included, is generated, and CO will react with NO in the flue gas. Zheng et al. [36] found that CaO has a strong catalytic effect on the reduction reaction of NO . The effect of CO on the reduction of NO in the decomposition furnace should be considered in the decomposition furnace due to the massive decomposition of raw $CaCO_3$, which has a high content of CaO .

The catalytic reduction reaction and its reaction rate are demonstrated as



$$R_{NO+CaO} = 39,816 \times 10^8 \rho_g Y_{CO} Y_{NO} e^{-8920/T_g} \quad (39)$$

2.2.9. Mathematical Model Coupling Strategy

The gases inside the furnace are defined as the main phase, including fuel volatile matter, O_2 , CO_2 , H_2O , N_2 , HCN , NO , and CO . The $CaCO_3$ and CaO are treated as the secondary phase and the fuel particles are the discrete phase. The main phase is the continuous phase in the combustion reaction, and the coupling between the fuel particles and the main phase is realized based on particle motion control equation. The reaction of volatile components is completed in the component transport equation of the main phase, in which S_{HCN} , S_{NO} , and S_{CO} are customized source terms. The S_{HCN} reaction rate is determined by the combustion reaction rate and Equations (34) and (37). The S_{NO} reaction rate is determined by Equations (34), (37) and (39), and the reaction rate of S_{CO} is determined only by the rate of the combustion reaction.

After the raw material enters the decomposition furnace, the energy Q_V is absorbed from the main phase by convection, conduction, and radiation. At the same time, the $CaCO_3$ decomposition reaction produces the enthalpy change Q_S , and the energy coupling between the raw material particles and the main phase is realized by adding Q_V and Q_S to the source term of the energy equation of the main phase. $\dot{m}_{CaCO_3-CaO}^{CaO}$ and $\dot{m}_{CaCO_3-g}^{CO_2}$ are the $CaCO_3$ -to- CaO mass transfer source terms and the $CaCO_3$ -to-main-phase mass transfer source terms, respectively. They are added to the interphase mass transfer source terms in the component transfer equation to complete the mass coupling process between the phases involved in the raw material decomposition reaction.

$$\dot{m}_{CaCO_3-CaO}^{CaO} = R \times M_{CaO} \quad (40)$$

$$\dot{m}_{CaCO_3-g}^{CO_2} = R \times M_{CO_2} \quad (41)$$

where R is the raw material decomposition reaction rate, determined by Equation (31). M_{CaO} and M_{CO_2} are the molecular molar masses of CaO and CO_2 . The coupling relationship between the phases is shown in the following Figure 2.

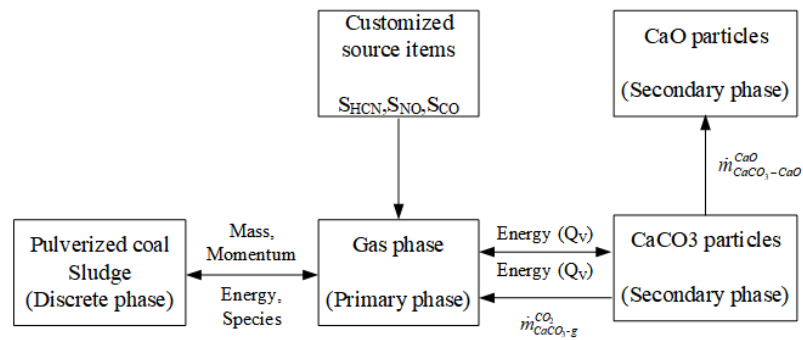


Figure 2. Decomposition furnace internal phase coupling relationship.

The ANSYS FLUENT software package R2020 is used in this work and the user-defined function (UDF) with an in-house code is applied to achieve the coupled simulations.

2.3. Simulation Conditions

2.3.1. Physical Properties of Materials and Component Composition of Gas

The elemental analysis, industrial analysis, and calorific value of coal dust and sludge are shown in Table 2. Table 3 gives the particle size distribution of coal dust particles, and the composition of kiln exhaust gas is listed in Table 4.

Table 2. Proximate analysis and element of fuels.

Samples	Industrial Analysis (wt%, ar)				Element Analysis (wt%, daf)				Lower Calorific Value (J/kg)
	M	V	FC	A	C	H	O	N	
Coal	3.45	22.15	57.30	17.10	79.55	4.30	15.20	0.95	2.5×10^7
Sludge	45	22	9	24	52.5	7.5	35	5	7.11×10^6

Table 3. Particle size distribution of coal dust particles.

Particle diameter (um)	0.4	1.2	3.6	10.8	28.3	85.3	averaged
Fraction (%)	1.1	4.2	12	21.6	38.5	22.6	33

Table 4. Composition of kiln exhaust flue gas.

Components	CO ₂	O ₂	H ₂ O	N ₂	CO	NO
Volume fraction (%)	19	1.4	1.5	76	2	0.08

2.3.2. Boundary Conditions for Walls and Each Inlet and Outlet

The boundary conditions employed in this work are averaged measured values under working conditions after the cement production line is thermally calibrated. The flow rate of the tertiary air and the flue gas at the kiln end is, respectively, 665,280 m³/h and 575,865 m³/h. The feed rate of raw meal is 420 t/h, and the total input of fuel is 5.6 kg/s. The speed of flue gas at the kiln end and the tertiary air inlet is calculated according to the inlet size and flow rate. There are four raw meal inlets and four pulverized coal inlets (fuel inlets) as illustrated in the geometry model, and the amount of raw meal and fuel are evenly distributed. Table 5 shows the boundary conditions for each inlet and outlet.

Table 5. Boundary conditions used for each inlet and outlet simulation.

Boundary Name	Boundary Type	Hydraulic Diameter (mm)	Speed (m/s)	Mass Flow Rate (kg/s)	Temperature (K)	Pressure (Pa)
Kiln end flue gas inlet	Speed inlet	2800	26	41.5	1440	−400
Tertiary air inlet	Speed inlet	2464	27	43	1360	−485
Raw material inlet 1,2,3,4	Mass flow inlet	800	/	29	1060	/
Fuel inlet 1,2,3,4	Discrete phase inlet	/	5	1.33	350	/
Decomposing furnace outlet	Pressure outlet	5800	/	/	/	−1500

The boundary condition of no_slip condition is adopted for the walls in the simulation of this paper. The internal and external heat exchange of the decomposition furnace is very little due to the presence of refractory bricks and insulation materials in the inner wall of the furnace. However, its heat dissipation also needs to be considered, so the convective heat transfer boundary condition is chosen for the thermal wall boundary condition.

2.3.3. Numerical Solution and Mesh Check

The simulation strategy is as follows. Since the corresponding chemical reactions such as combustion and decomposition would happen after the discrete phases like coal powders, sludge, and raw material particles enter into the decomposition furnace, a two-step solution strategy is adopted. Firstly, the cold flow field for each gas phase mixing and flowing in the decomposition furnace is simulated. Then, the discrete phases such as coal powder, sludge, and raw material particles will be injected into the decomposition furnace after the cold flow field is stabilized. After each of the above discrete phases is injected, the computation of their interaction with other phases and chemical reactions starts until the solution of the final thermal flow field is obtained.

The pressure-based solver is applied for steady-state calculations. The coupled algorithm is used to couple the pressure–velocity of the discrete system of equations. The momentum and turbulent kinetic energy are solved in a discrete format of first-order windward. The residuals for the energy term are set to be less than 10^{-6} , and the residuals for the rest of the terms are set to be less than 10^{-3} . It takes about 12 h in an Intel Xeon Gold 6238R workstation with 128 cores to finish a calculation.

A mesh independence check is necessary in simulations. Figure 3a shows the mesh of the whole decomposition furnace system, which adopts a polyhedral unstructured mesh. For the complex structure of the coal injection pipe and other small-sized locations, shrinkage and other size changes in the location of the grid are carried out for a local refinement operation to ensure the accuracy of the calculation. In this work, the grid independence of the mesh used in the calculation is verified. Figure 3b gives the gas temperatures at the outlet under different mesh numbers. Consequently, the final number of the body mesh of the whole decomposition furnace system is determined as 380,000, with good overall uniformity and low skewness of the mesh, which meets the grid independence demand.

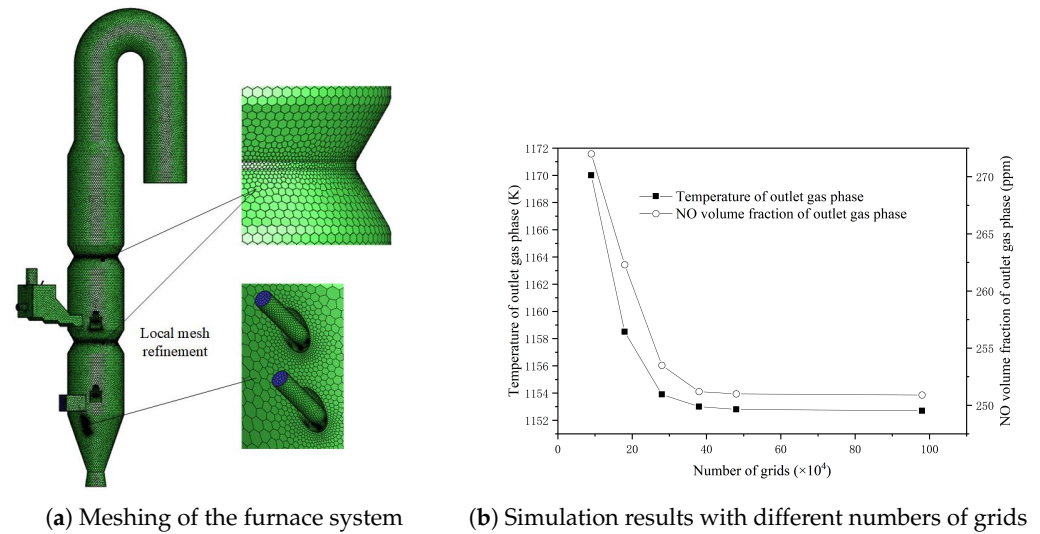


Figure 3. Grids for decomposition furnace system and their independence check.

3. Results and Discussions

3.1. The Combustion Process without Sludge Involved

Firstly, numerical simulations for the decomposition furnace without sludge were carried out, and related data in the field were collected to verify the model used.

3.1.1. The Simulated Flows in the Furnace System

Figure 4 shows the temperature distribution of different cross-sections. It can be seen that the temperature of the decomposition furnace's lower section of the first column area is the highest. This area is the main combustion zone. This is because the coal powder injecting from the lower part of the furnace cone body flows upward with the kiln exhausted flue gas and meets the tertiary air. Then, they move together and violent combustion reactions happen along with oxygen gas, resulting in the highest temperature of 2000 K or so. Once the raw materials enter into the furnace from a raw material spreading box, the decomposition starts. In the vicinity of the spreading box, there is a relatively low-temperature region. As the height in the furnace increases, the decomposition rate of the raw material reduces to a certain degree. The heat and mass transfer processes become more complete, and the gas steam temperature in the furnace is maintained in a certain range. The final averaged temperature of the gas phase at the outlet cross-section of the decomposition furnace can be obtained as 1145.2 K.

Figure 5 shows the distribution of NO_x in the decomposition furnace. It can be found that the highest NO_x volume fraction is at the bottom of the decomposition furnace, which is as high as 800 ppm. At the height of 0–4 m, the NO_x content changes less because only kiln flue gas enters into the furnace in this area. At 4–20 m, the NO_x volume fraction shows a decreasing trend. This is due to the fact that the tertiary air in this region starts to mix with the coal dust that rises with the flue gas, and a large amount of volatile matter and the gases generated by its combustion dilute the volume fraction of NO_x introduced from the kiln tail flue gas. For the 24–36 m height region, the volatile matter volume fraction decreases gradually. At the same time, a part of NO_x is generated, and the content of NO_x is basically unchanged after 36 m. Combining Figures 4 and 5, it can be revealed that volatile fraction concentration and temperature are the main factors affecting the NO_x generation rate. The average molar volume fraction of NO_x at the decomposition furnace outlet is about 214 ppm.

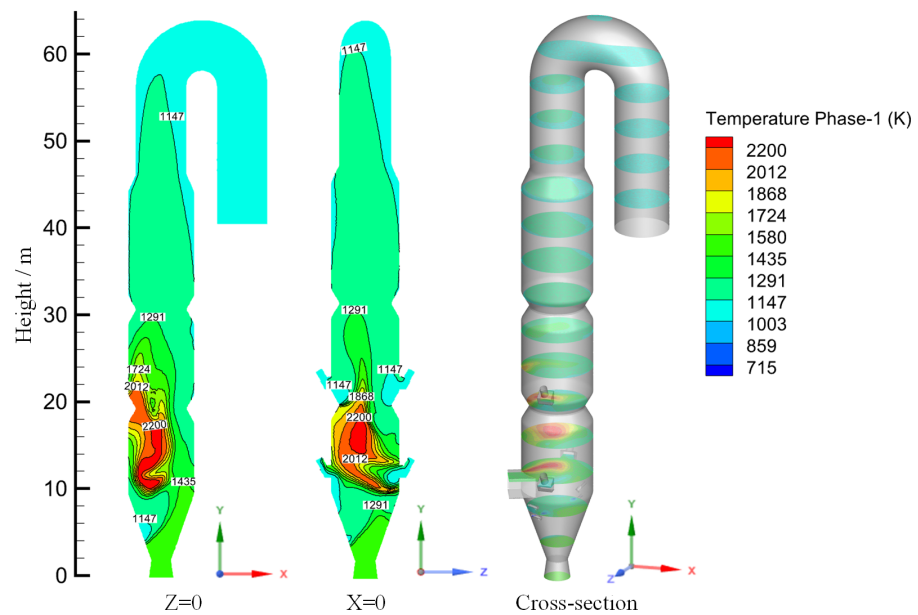


Figure 4. The temperature distributions in the furnace.

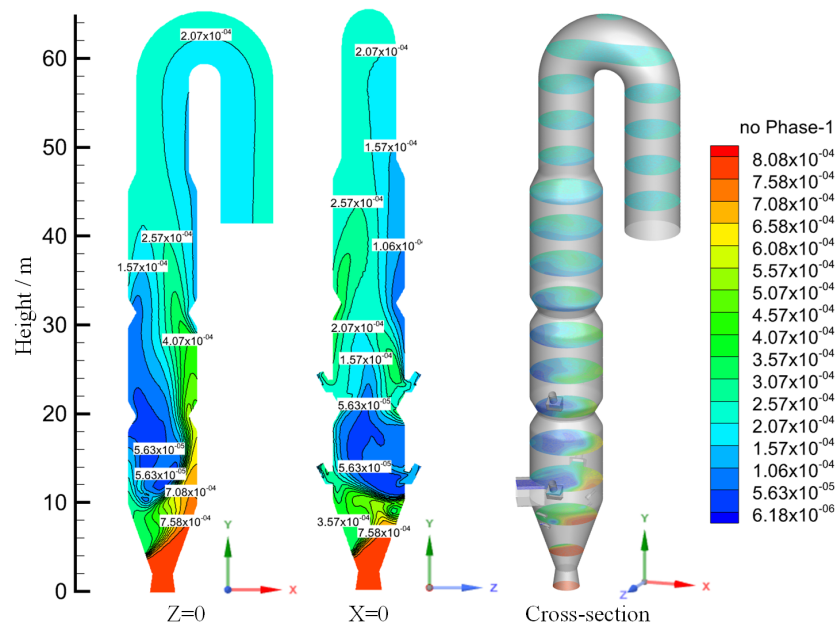


Figure 5. The NOx distributions inside the decomposition furnace.

Figure 6a–d show the volume fractions of O_2 , CO_2 , volatile fraction, and $CaCO_3$, respectively. From Figure 6, it can be seen that the distributions of the four aspects are basically consistent with the temperature and component fields mentioned above. Combining Figure 4 with Figure 6a,c, a high-temperature zone occurs at the location of high volatile matter concentration and rapid O_2 depletion, which is due to the combustion of volatile matter at this location. From Figure 6b,d, it can be found that there is a certain relationship between $CaCO_3$ and CO_2 distribution. There is a piece of the raw material aggregation area at the decomposition furnace cone, where a large amount of heat absorption and decomposition of raw materials happen, resulting in the generation of CO_2 and forming a

local low-temperature zone. This also coincides with Figure 4. The mass flow rate of $CaCO_3$ at the outlet section of the decomposition furnace is 9.06 kg/s, while the initial $CaCO_3$ mass flow rate is 92 kg/s. Then, the decomposition rate of raw meal in the decomposition furnace can be calculated as 90.2%.

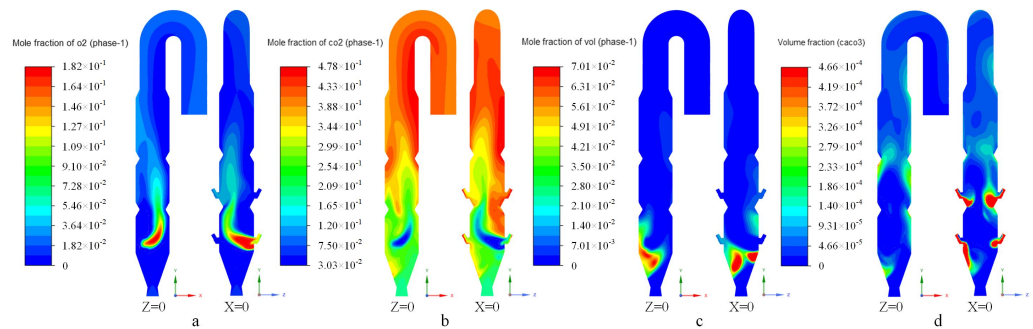


Figure 6. Volume fraction distributions of (a) O_2 , (b) CO_2 , (c) volatile component, and (d) $CaCO_3$ in the decomposition furnace.

3.1.2. Model Verification

Field operation data of the cement decomposition furnace system were collected in order to verify the model in this work. Table 6 lists the applied measuring instruments made in China. The NOVAPLUS multifunctional flue gas analyzer and Laoying 3012H automatic smoke tester were used to measure the atmosphere composition of the flue gas, the tertiary air, and the outlet of the cement decomposition furnace. A single platinum–rhodium thermocouple was applied to measure the gas-phase temperature. An anti-clogging Pitot tube and a three-parameter detector were employed to measure the dynamic and static pressure of the inlet and outlet. Before and after the measurements, a gas tightness check was carried out for the instruments. Moreover, the measured results were also calibrated in order to ensure the accuracy of collected data. Figure 7 shows a physical diagram of each examining instrument used along with a photograph of the decomposition furnace field site.

Table 6. Detailed information of the measuring instruments.

Instrument Name	Type	Manufacturer	Place of Production
Multifunctional Gas Analyzer Single	NOVAPLUS	MRU Company	Beijing, China
Platinum–Rhodium Thermocouple	WRNK-104	Shanghai Shenjie Instrument Company	Shanghai, China
Three-Parameter Tester	FST-685	Changchun Lemei Technology Company	Changchun, China
Automatic Smoke Tester	Laoying 3012H	Qingdao Laoying Environmental Technology Company	Qingdao, China
Anti-clogging Pitot Tube	PTS-8-3000	Beijing Beituo Instrument Equipment Company	Beijing, China

To improve the accuracy of the measured boundary conditions, the data in each section were averaged from six sets of data recorded at nine different sampling points. These points were chosen to avoid the bends, deformations, and gates preventing the effects of eddy currents and wind leakage. Figure 8 shows the schematic diagram of the sampling points selected. At the outer and middle of the section, there are eight points uniformly distributed in two concentric rings. The rings are 2/3 and 1/3 times the diameter of the cross-section, respectively, and there is one more at the very center of the cross-section.

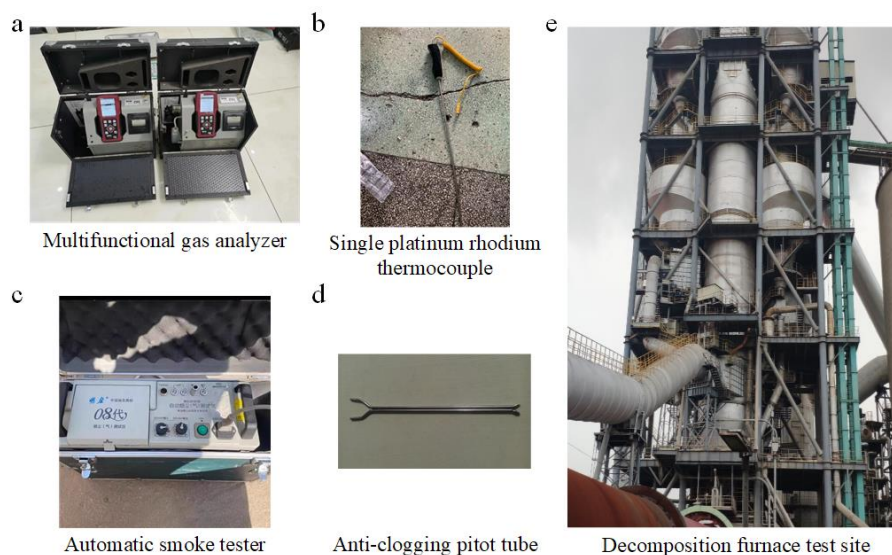


Figure 7. The test instruments of (a) Multifunctional gas analyzer, (b) Single platinum rhodium thermocouple, (c) Automatic smoke tester, (d) Anti-clogging pitot tube and (e) the field site photo.

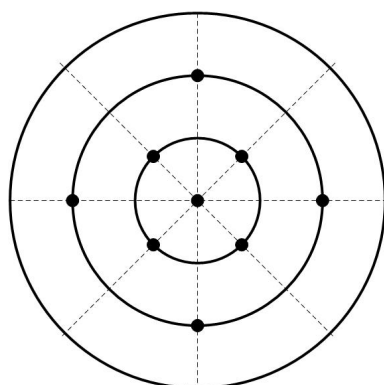


Figure 8. Schematic diagram of sampling points at a cross-section.

Then, the data averaged from the nine sampling points are treated as an effective measurement. Six measurements are obtained and listed in Table 7. Table 8 shows the comparison between the simulated results and the field measurements. It can be found that the employed numerical model could accurately predict the combustion, raw material decomposition, and generation and reduction of NO_x in the decomposition furnace. Therefore, it could be further used for investigating the co-processing combustion with sludge involved.

Table 7. Measurements of running parameters.

No.	Average Outlet Temperature (K)	Volume Fraction of NO at Outlet (ppm)	Raw Meal Decomposition Rate (%)
1	1143.1	225	90.8
2	1141.8	228	91.2
3	1138.5	216	92.1
4	1137.3	218	92.6
5	1142.5	223	91.5
6	1137.8	220	91.7

Table 8. Comparison between numerical simulation results of decomposition furnace and on-site measured values.

	Average Outlet Temperature (K)	Volume Fraction of NO at Outlet (ppm)	Raw Meal Decomposition Rate (%)
Average of actual measurements	1140.2	222	91.7
Numerical simulation value	1145.2	214	90.2
Relative error	0.43%	3.60%	1.64%

3.2. The Co-Processing Combustion Characteristics with Sludge Involved

Xiao et al. [37] sorted out the emission process of *NO* during the co-disposal of sludge in the cement industry, and proposed that parameters like sludge input and sludge particle size have an influence on the decomposition of raw materials and the generation of *NO*. In this work, we concentrate on the effects of key parameters on the decomposition furnace characteristics like raw material decomposition rate and *NO* emission. Three perspectives, namely sludge mixing ratio, preheating furnace arrangement height, and sludge particle size, are focused on and explored.

3.2.1. Effect of the Mixing Ratio of Municipal Sludge

The sludge mixing ratio has a significant impact on the decomposition. The mix ratios of 5%, 10%, 15%, and 20% are compared. The mixing ratios of different pulverized coal and municipal sludge and the mass flow rate of the fuel are shown in Table 9. The rest of the parameters include a preheating furnace arrangement height of 21.5 m and sludge particle size of 1.0 mm.

Table 9. Mass flow rate of coal powder and municipal sludge under different mixing ratios.

Mixing Ratio of Municipal Sludge (%)	Pulverized Coal Mass Flow Rate (kg/s)	Municipal Sludge Mass Flow Rate (kg/s)
5	5.32	0.28
10	5.04	0.56
15	4.76	0.84
20	4.48	1.12

Figure 9 gives the temperature distributions under different sludge mixing ratios. The averaged gas-phase temperatures of the exit section of the decomposition furnace for the mixing ratios from 5% to 20% were 1157.4 K, 1153.9 K, 1153.6 K, and 1150.4 K. Figure 10 shows the distribution curves of the concentrations of *NO*, *CaCO₃*, and *CaO* in the y-section at different heights for the changed ratios. It can be found from Figure 10a that sludge mixing could improve the concentration of *NO* to a certain degree at the outlet, and the overall trend of all mixing ratios is kept the same. In the range of 20–28 m, the hot air and municipal sludge thus enter the decomposition furnace, and the *NO* volume fraction shows a decreasing and then increasing trend. In the range of 28–36 m, the *NO* volume fraction rises slowly, and it remains basically unchanged in the range from 36 m to the furnace outlet, which indicates that the generation and reduction of *NO* have been completed. From Figure 10b,c, we can see that the distribution of the *CaCO₃* and *CaO* concentration is basically the same as that in the case of non-sludge, and the volume fraction of *CaCO₃* has two great values around 12 m and 24 m, which are caused by the graded entry of raw material into the furnace. The *CaCO₃* volume fraction in the range of 12–28 m drops sharply to a minimum value at 20 m, and, at the same time, the volume fraction of *CaO* rises faster, which demonstrates that the decomposition reaction of the raw material in this range is more intense. The decomposition reaction is basically completed in the range from 28 m to the furnace outlet.

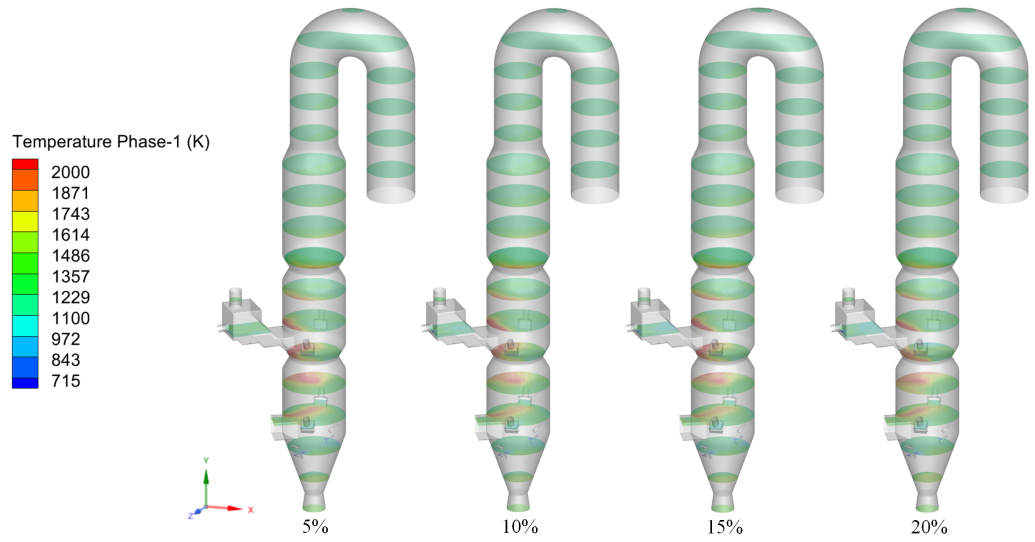
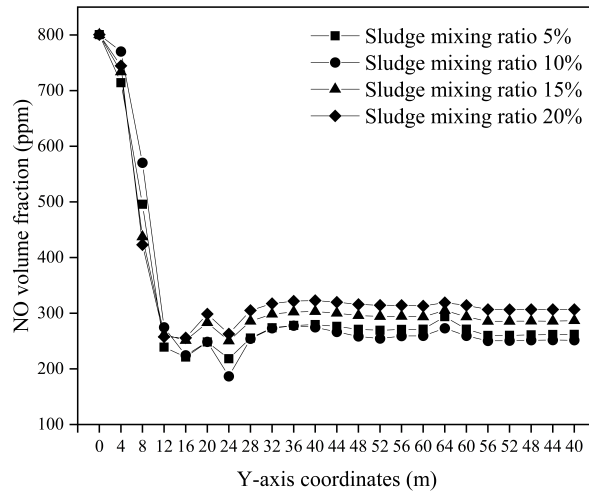
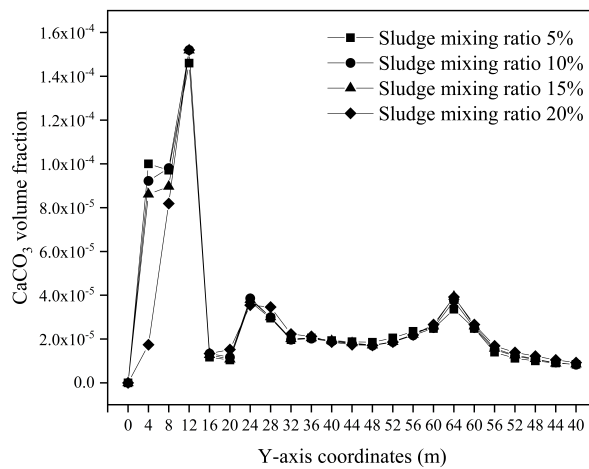


Figure 9. The temperature distributions under different sludge mixing ratios.

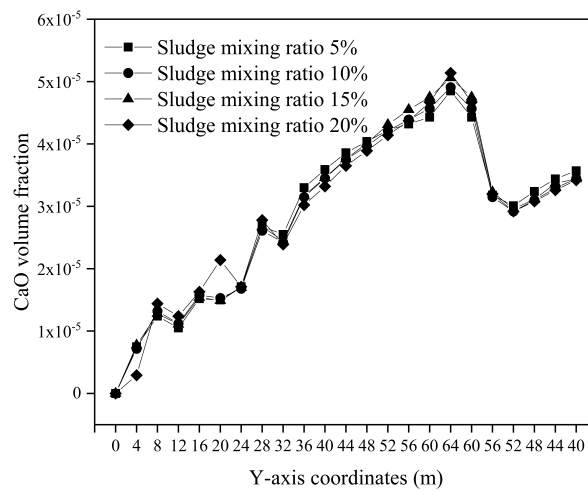


(a) NO volume fraction under different sludge mixing ratios.



(b) CaCO₃ volume fraction under different sludge mixing ratios.

Figure 10. Cont.



(c) CaO volume fraction under different sludge mixing ratios.

Figure 10. Volume fractions under different sludge mixing ratios.

Figure 11 exhibits the raw material decomposition rate and the outlet NO volume fraction at different sludge mixing ratios. The raw material decomposition rate of the decomposition furnace outlet section was 89.8%, 89.9%, 89.6%, and 88.6% at the mixing ratios of 5%, 10%, 15%, and 20% of the municipal sludge, and the NO volume fractions at the outlet were 271 ppm, 251 ppm, 287 ppm, and 307 ppm, respectively. When the mixing ratio was changed from 5% to 20%, the raw material decomposition of the decomposition furnace increased and then decreased. It reached at a maximum value of 89.9% when the mixing ratio was 10%. At the same time, the volume fraction of NO exported from the decomposition furnace had a minimum value of 251 ppm. Combining these results, 10% was taken as the preferable mixing ratio of municipal sludge for the decomposition furnace.

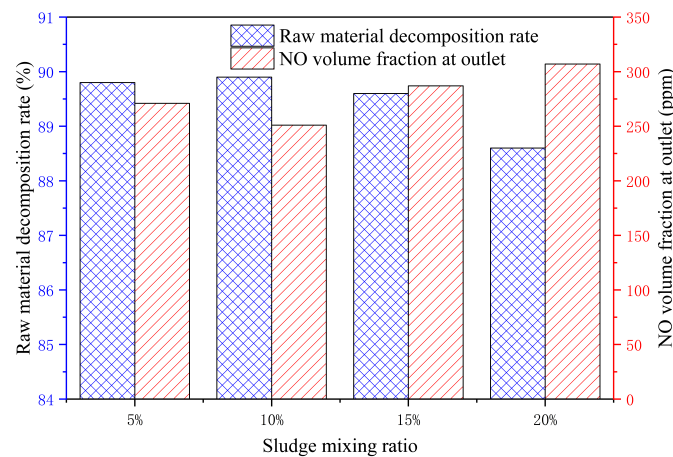


Figure 11. The raw material decomposition rate and NO fraction at outlet under different sludge mixing ratios.

3.2.2. Effect of the Height of the Preheating Furnace

Where to feed sludge into the furnace is another significant parameter for co-processing. According to the furnace structure, the sludge inlet can be set at the upper and lower parts near the two throats of the furnace, which can be found in Figure 12. Four heights, i.e., 15.5 m, 21.5 m, 26.5 m, and 33.5 m, between the preheating furnace and the kiln end flue gas inlet are compared. Remained parameters like the sludge mixing ratio of 10% and sludge particle diameter of 1.0 mm are kept as unchanged.

Figure 12 reveals the temperature distributions under different preheating furnace heights. The final averaged temperatures at the decomposition furnace outlet at the 15.5 m, 21.5 m, 26.5 m, and 33.5 m heights were, respectively, 1152.7 K, 1153.9 K, 1152 K, and 1151.6 K. Figure 13 shows the distribution curves of the concentrations of NO , $CaCO_3$, and CaO . It can be seen from Figure 13a that the overall trend of the NO volume fraction for the four heights is approximately the same. All the four curves have large fluctuations in the NO volume fraction at 16–20 m, 20–24 m, 28–32 m, and 32–36 m, respectively, which also coincides with the preheating furnace height. From Figure 13b,c, it can be noticed that the higher the preheating furnace is installed, the smaller the impact on the main combustion zone of the decomposition furnace cone body. And, the raw material decomposition reaction is more concentrated at about 16–20 m, which is the middle of the first part of the furnace. As the preheating furnace height decreases, the raw material decomposition reaction would also transfer and concentrate at about 20–24 m, which is at the middle of the second part of the decomposition furnace.

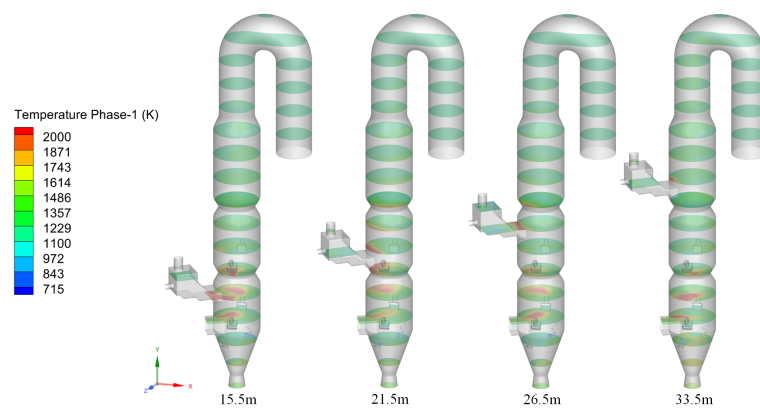
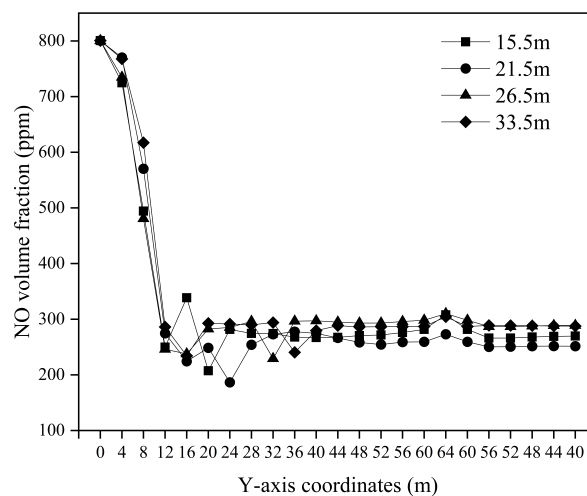


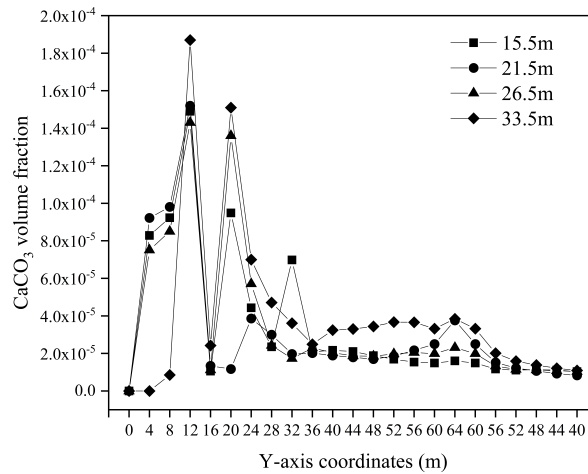
Figure 12. Temperature distributions under different preheating furnace heights.

Different preheating furnace heights have an influence on the NO volume fraction and raw material decomposition rate at the decomposing furnace outlet. From 15.5 m to 33.5 m, the NO volume fraction at the outlet decreases and then increases, and the raw material decomposition rate rises first and then descends. With the change in preheating furnace arrangement, the hot air and sludge enter into the decomposition furnace in different locations, resulting in a changed local temperature field, which would impact the NO generation and the raw material decomposition reactions.

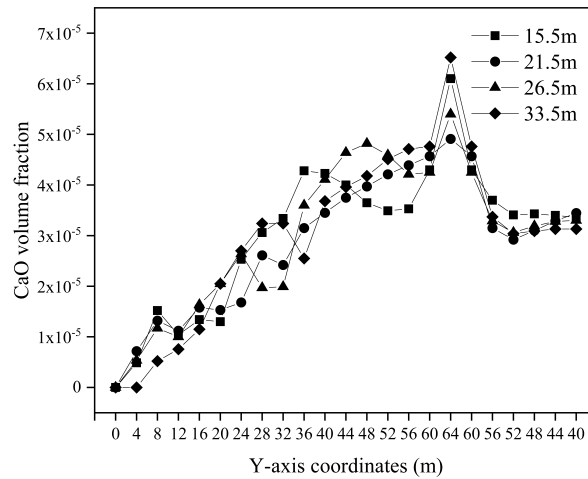


(a) NO volume fraction under different preheating furnace heights.

Figure 13. Cont.



(b) CaCO₃ volume fraction under different preheating furnace heights.



(c) CaO volume fraction under different preheating furnace heights.

Figure 13. Volume fractions under different preheating furnace heights.

Figure 14 presents the raw material decomposition rate and NO volume fraction under different preheating furnace heights. The decomposition rates at the decomposing furnace outlet are 87.7%, 89.9%, 87.5%, and 87.4%, respectively, under the heights of 15.5 m, 21.5 m, 26.5 m, and 33.5 m, and those of the NO fractions are 270 ppm, 251 ppm, 289 ppm, and 288 ppm, respectively. When the preheating furnace is arranged at 21.5 m, the raw material decomposition rate reaches a maximum value of 89.9% and the NO fraction also obtains a minimum value of 251 ppm. Consequently, 21.5 m is an effective height for the preheating furnace for feeding sludge.

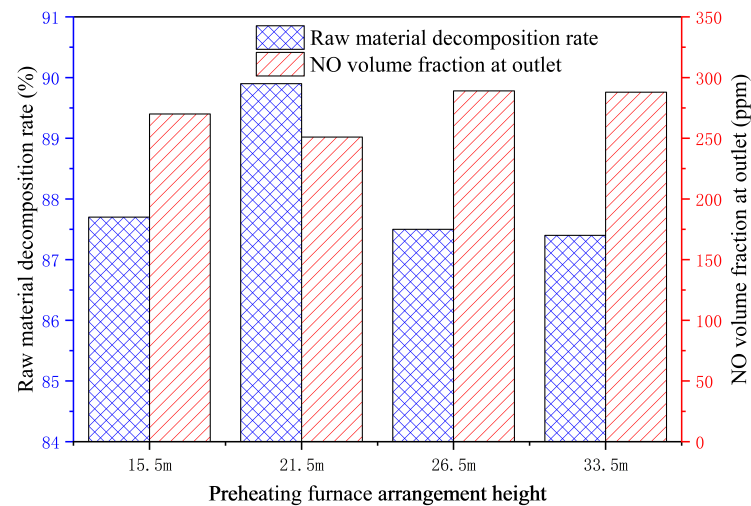


Figure 14. Raw material decomposition rate and NO fraction at outlet under different preheating furnace heights.

3.2.3. Effect of the Municipal Sludge Size

Sludge size is an important operating parameter that remarkably affects the whole co-processing technique. In this work, sludge particle diameters of 0.5 mm, 1 mm, 3 mm, and 5 mm were compared. The sludge mixing ratio of 10% and the preheating furnace height of 21.5 m were kept as unvaried.

Figure 15 exposes the temperature distributions under different sludge particle diameters. It can be noticed that the smaller the sludge particles are, the closer the combustion zone is to the sludge inlet. The sludge is partially burned in the preheating furnace when the particle size is 0.5 mm, while the sludge combustion is concentrated in the middle of the decomposition furnace cylinder when the particle size is 5 mm.

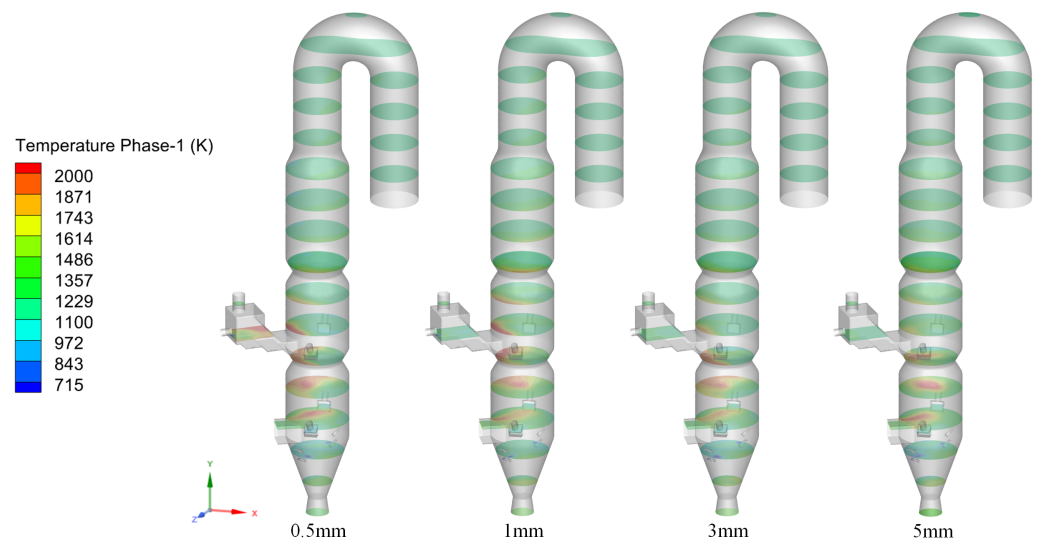


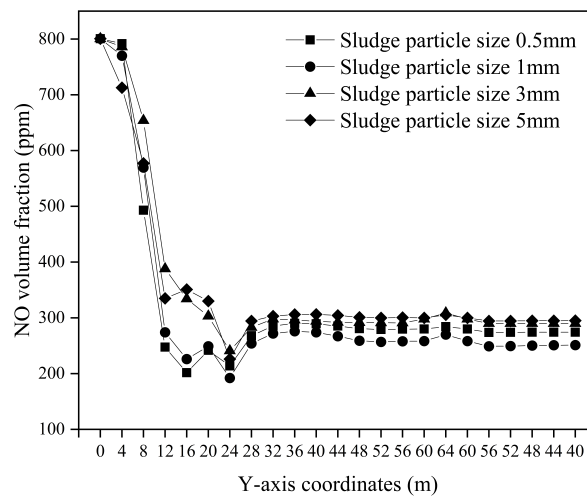
Figure 15. Temperature distributions under different sludge particle diameters.

The final average gas-phase temperatures at the furnace outlet ranging from 0.5 mm to 5 mm were 1153.9 K, 1151.7 K, 1146.2 K, and 1144.5 K. It can be seen from Figure 16a that the NO volume fraction at the furnace outlet increases and then decreases when the sludge particle sizes ranges from 0.5 mm to 5 mm.

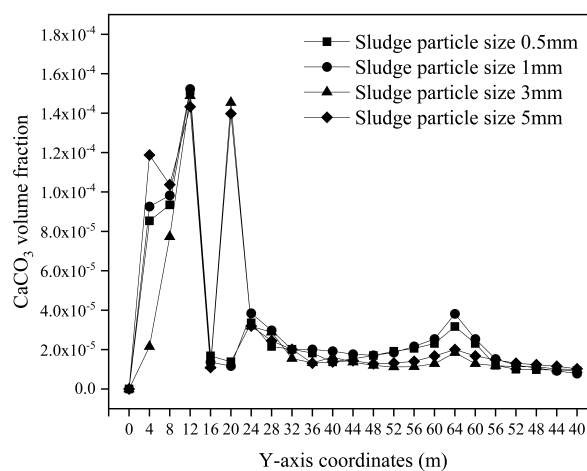
Generally, the NO concentration in the furnace has the lowest value when the sludge particle size is 1.0 mm compared with the other three particle sizes. As can be seen in Figure 15, when the particle size is smaller, like 0.5 mm in the simulation, a portion of the

sludge is burned completely in the preheating furnace due to the small particle size. This makes the temperature field inside the decomposition furnace at 0.5 mm different from the other cases, which in turn affects the reaction rate of NO_x consumption. When the particle is larger, the sludge would burn more difficultly and react more slowly with oxygen. The oxygen content in the furnace was more than that in the case of small particle sizes. The intermediate product, HCN , in the competition reaction between O_2 and NO was at a competitive advantage in the reaction of generating NO , and was at a disadvantage in consuming NO . Consequently, in the range of 12–24 m, the 3 mm and 5 mm conditions produce more NO than the other two situations. The reaction of producing and consuming NO has been basically completed after 28 m.

Due to the large sludge size, the time taken to finish three steps, i.e., water evaporation, volatile analysis and combustion, and coke combustion, is greater. The burning is more difficult. This would affect the sludge particle combustion rate and lead to, on the contrary, a smaller increase in the NO volume fraction for the two conditions of 3 mm and 5 mm. As can be seen in Figure 16b,c, the locations of the raw material reaction occurring at the four sludge particle sizes are roughly the same. Moreover, the larger the particles are, the closer they are to the preheating furnace for the raw material reactions, namely at 21.5 m in these cases.

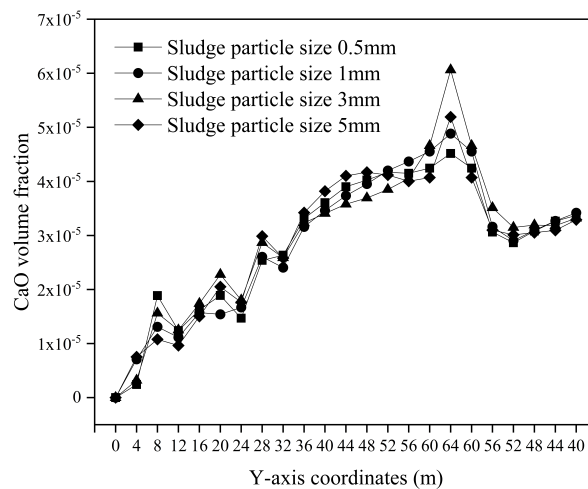


(a) NO volume fraction under different sludge particle diameters.



(b) $CaCO_3$ volume fraction under different sludge particle diameters.

Figure 16. Cont.



(c) CaO volume fraction under different sludge particle diameters.

Figure 16. Volume fractions under different sludge particle diameters.

Figure 17 summarizes the raw material decomposition rate and the NO volume fraction under different sludge sizes. It can be found that when the sludge particle sizes were 0.5 mm, 1 mm, 3 mm, and 5 mm, the final NO volume fractions at the decomposition furnace outlet were 273 ppm, 251 ppm, 290 ppm, and 295 ppm, and the raw material decomposition rates were 88.6%, 89.9%, 88.1%, and 87.8%, respectively. The decomposition rate reached a maximum value of 89.9% and the NO fraction hit a minimum value of 251 ppm, as well as when the particle size stayed at 1.0 mm. Based on the results, 1.0 mm could be an effective sludge size for co-processing combustion.

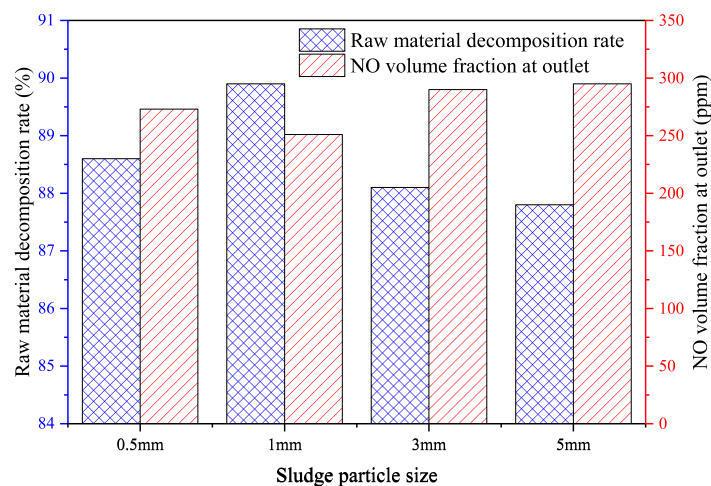


Figure 17. Raw material decomposition rate and NO fraction at outlet under different sludge diameters.

4. Conclusions

In this study, computational fluid dynamics were utilized to investigate the co-processing combustion characteristics of sludge within an industrial 6000 t/d cement decomposition furnace. Three aspects, including sludge mixing ratio, preheating furnace arrangement height, and sludge size, have been focused on for their effects on the furnace combustion, NO_x generation, and raw material decomposition reactions via a verified numerical model. The main conclusions can be drawn as follows.

(1) The relative errors between the simulated results of the decomposition furnace and the corresponding measured data from the field, including the average temperature, the

volume fractions of *NO* at the furnace outlet, and the raw material decomposition rate, were all within 5%, which verified the reasonableness of the applied numerical model.

(2) Sludge in the preheating furnace mainly undergoes two stages, including water evaporation and volatilization component separation. The main combustion still happens in the decomposition furnace. The mixing ratio of municipal sludge increased from 5% to 20%, and the raw material decomposition rate reached a maximum value of 89.9% when the mixing ratio was 10%, which improved the raw material decomposition rate by 1.3% compared with the minimum. At the same time, the *NO* volume fraction at the furnace outlet reached a minimal value of 251 ppm, which decreased by 56 ppm compared with the maximum.

(3) The preheating furnace height has an effect on the volume fraction of *NO* at the furnace outlet. When the height increases from 15.5 m to 33.5 m, the volume fraction of *NO* exported from the decomposition furnace decreases first and then increases. It reached a minimal value of 251 ppm when the preheating furnace was installed at 21.5 m, which is reduced by 37 ppm compared to the maximum.

(4) The particle size of the municipal sludge has a great influence on the volume fraction of *NO* exported from the decomposition furnace. When the sludge size was enhanced from 0.5 mm to 5 mm, the volume fraction of *NO* exported from the decomposition furnace decreased first and then increased. The *NO* volume fraction exported from the furnace was at a minimal value of 251 ppm when the particle size of the sludge was 1.0 mm, which is 44 ppm lower than the maximum.

An optimized parameter combination for the mixing ratio, preheating furnace height, and sludge size through related methods like orthogonal experiment designs would be further carried out at the next level.

Author Contributions: Conceptualization, L.Z. and Y.M.; methodology, L.Z. and K.L.; software, L.Z.; validation, Y.M. and L.Z.; formal analysis Y.M., L.Z. and K.L.; investigation, L.Z., K.L. and C.T.; resources, Q.X. and Y.M.; data curation, L.Z., K.L. and Q.L.; writing—original draft preparation, L.Z.; writing—review and editing, Q.X., Y.M. and Q.L.; visualization, L.Z., Q.X., K.L., Q.L. and C.T.; supervision, Y.M. and Q.X.; project administration, Y.M. and Q.X.; funding acquisition, Y.M. All authors have read and agreed to the published version of the manuscript.

Funding: This research received no external funding.

Institutional Review Board Statement: Not applicable.

Informed Consent Statement: Not applicable.

Data Availability Statement: The data are available from the corresponding author on reasonable request.

Conflicts of Interest: The authors declare no conflicts of interest.

Abbreviations

CO	Carbon monoxide
CO ₂	Carbon dioxide
CaO	Calcium oxide
CaCO ₃	Calcium carbonate
H ₂ O	Water
HCN	Hydrogen cyanide
NO	Nitrogen oxide
NO _x	Nitric oxide
NH ₃	Ammonia
N ₂	Nitrogen
O ₂	Oxygen
CFD	Computational Fluid Dynamics
EMMS	Energy-Minimization Multi-Scale
DO	Discrete Ordinate

Nomenclature

d_1	Kiln end flue gas inlet diameter	mm
d_2	Decomposition furnace column combustion chamber diameter	mm
d_3	Decomposition furnace internal indentation diameter	mm
d_4	Decomposition furnace outlet diameter	mm
d_5	Inlet diameter of coal injection pipe	mm
d_6	Sludge inlet diameter	mm
d_7	Preheating furnace air inlet diameter	mm
d_8	Raw material inlet diameter	mm
l_1	Vertical distance between upper and lower coal injection pipes	mm
l_2	Vertical distance between upper and lower raw material discharging pipes	mm
l_3	Vertical distance between upper and lower grates	mm
h_1	Height of lower coal injection pipe	mm
h_2	Height of lower raw material discharging pipes	mm
h_3	Height of preheating furnace arrangement position	mm
h_4	Decomposition furnace height	mm
θ_1	Angle between coal injection pipe and raw material discharging pipes	°
θ_2	Angle between preheating furnace and raw material discharging pipes	°
θ_3	Angle between coal injection pipe and horizontal plane	°
θ_4	Angle between raw material discharging pipes and horizontal plane	°
α	Phase volume fraction	1
ρ	Density of each phase	kg/m^3
u	Velocity of each phase	mm
\dot{m}_{sg}	Mass transmission from sorbent phase to gas phase	kg
\dot{m}_{sp}	Mass transmission from sorbent phase to product phase	kg
\vec{g}	Gravitational acceleration	m/s^2
$\vec{\tau}$	Stress tensor	Pa
μ	Shear viscosity	Pa-s
λ	Turbulent eddy viscosity	Pa-s
\vec{F}	The additional force	N
$m_p \frac{\vec{u}_g - \vec{u}_p}{\tau_r}$	Drug force	N
C_d	Drug coefficient	1
k	Turbulent kinetic energy	J
ε	Turbulent dissipation rate	1
μ_t	Turbulent eddy viscosity	Pa-s
q_r	Radiative heat flux	W/m^2
a	Absorption coefficients	m^{-1}
σ_s	Scattering coefficient	m^{-1}
k_1	Competing volatilization rates at low temperatures	s^{-1}
k_2	Competing volatilization rates at high temperatures	s^{-1}
R_1	Coke combustion diffusion rate	s^{-1}
R_2	Coke combustion kinetic rate	s^{-1}
E	Activation energy	kJ/mol
D_p	Coke particle diameter	mm
T_p	Coke particle temperature	K
T_∞	Atmosphere temperature around coke particles	K
p	Partial pressure of gas around coke particles	Pa
Y_i	Mass fraction of substance i	1
$M_{w,i}$	Molecular mass of component i	g
R_i	Net rate of production of a chemical reaction	s^{-1}

S_i	Additional generated rates due to discrete phases and user-defined source terms	s^{-1}
\vec{J}_i	Diffusion flux of component i	$kmol/m^3$
$R_{i,r}$	Chemical reaction rate of component i in reaction r	s^{-1}
$V'_{i,r}$	Stoichiometry of reactant i in reaction r	1
$V''_{j,r}$	Stoichiometry of product j in reaction r	1
N_r	Total number of reactants	1
C_j	Molar concentration of reactants	mol/L
P_{CO_2}	Partial pressure of carbon dioxide	Pa
P_{eCO_2}	Equilibrium pressure of carbon dioxide as the decomposition reaction proceeds	Pa
ρ_g	Density of gas mixtures	kg/m^3
T_g	Temperature of gas mixtures	K
\dot{m}_{CaCO_3-CaO}	CaCO ₃ -to-CaO mass transfer source terms	1
\dot{m}_{CaCO_3-g}	CaCO ₃ -to-main-phase mass transfer source term	1

References

- Kor-Bicakci, G.; Eskicioglu, C. Recent developments on thermal municipal sludge pretreatment technologies for enhanced anaerobic digestion. *Renew. Sustain. Energy Rev.* **2019**, *110*, 423–443. [\[CrossRef\]](#)
- Nguyen, V.K.; Chaudhary, D.K.; Dahal, R.H.; Trinh, N.H.; Nguyen, D.D. Review on pretreatment techniques to improve anaerobic digestion of sewage sludge. *Fuel* **2020**, *285*, 119105. [\[CrossRef\]](#)
- Zhang, B.; Zhou, X.; Ren, X.; Hu, X.; Ji, B. Recent Research on Municipal Sludge as Soil Fertilizer in China: A Review. *Water Air Soil Pollut.* **2023**, *234*, 119. [\[CrossRef\]](#) [\[PubMed\]](#)
- Xu, J.; Ping, L.; Cao, H.; Liu, W.; Gu, Y.; Lin, X.; Huang, J. Application Status of Co-Processing Municipal Sewage Sludge in Cement Kilns in China. *Sustainability* **2019**, *11*, 3315. [\[CrossRef\]](#)
- Xu, S.; He, J.; Pei, F.; Li, K.; Dai, Z. Numerical Study on the Denitrification Efficiency of Selective Noncatalytic Reduction Technology in Decomposing Furnace. *J. Chem.* **2020**, *2020*, 9484683. [\[CrossRef\]](#)
- Valdes, C.F.; Marrugo, G.P.; Chejne, F.; Marin-Jaramillo, A.; Franco-Ocampo, J.; Norena-Marin, L. Co-gasification and tiontion of industrial solid waste mixtures and their implications on environmental emissions, as an alternative management. *Waste Manag.* **2020**, *101*, 54–65. [\[CrossRef\]](#) [\[PubMed\]](#)
- Magdziarz, A.; Werle, S. Analysis of the combustion and pyrolysis of dried sewage sludge by TGA and MS. *Waste Manag.* **2014**, *34*, 174–179. [\[CrossRef\]](#)
- Li, J.; Zhang, L.H.; Duan, F. Effect of the Dried and Hydrothermal Sludge Combustion on Calcium Carbonate Decomposition in a Simulated Regeneration Reactor of Calcium Looping. *Energy Fuels* **2020**, *34*, 4745–4753. [\[CrossRef\]](#)
- He, P.; Poon, C.S.; Tsang, D.C.W. Using incinerated sewage sludge ash to improve the water resistance of magnesium oxychloride cement (MOC). *Constr. Build. Mater.* **2017**, *147*, 519–524. [\[CrossRef\]](#)
- Wang, C.; Wang, X.; Jiang, X.; Li, F.; Lei, Y.; Lin, Q. The thermal behavior and kinetics of co-combustion between sewage sludge and wheat straw. *Fuel Process. Technol.* **2019**, *189*, 1–14. [\[CrossRef\]](#)
- Fang, P.; Tang, Z.-J.; Huang, J.-H.; Cen, C.-P.; Tang, Z.-X.; Chen, X.-B. Using sewage sludge as a denitration agent and secondary fuel in a cement plant: A case study. *Fuel Process. Technol.* **2015**, *137*, 1–7. [\[CrossRef\]](#)
- Lv, D.; Zhu, T.; Liu, R.; Lv, Q.; Sun, Y.; Wang, H.; Liu, Y.; Zhang, F. Effects of co-processing sewage sludge in cement kiln on NO_x, NH₃ and PAHs emissions. *Chemosphere* **2016**, *159*, 595–601. [\[CrossRef\]](#) [\[PubMed\]](#)
- Fang, P.; Tang, Z.; Xiao, X.; Huang, J.; Xiong, B. Using sewage sludge as a flue gas denitration agent for the cement industry: Factor assessment and feasibility. *J. Clean. Prod.* **2019**, *224*, 292–303. [\[CrossRef\]](#)
- Nakhaei, M.; Hessel, C.E.; Wu, H.; Grévain, D.; Zakrzewski, S.; Jensen, L.S.; Glarborg, P.; Dam-Johansen, K. Experimental and CPFD study of gas–solid flow in a cold pilot calciner. *Powder Technol.* **2018**, *340*, 99–115. [\[CrossRef\]](#)
- Mikulčić, H.; von Berg, E.; Vujanović, M.; Wang, X.; Tan, H.; Duić, N. Numerical evaluation of different pulverized coal and solid recovered fuel co-firing modes inside a large-scale cement calciner. *Appl. Energy* **2016**, *184*, 1292–1305. [\[CrossRef\]](#)
- Mikulčić, H.; Berg, E.V.; Vujanović, M.; Duić, N. Numerical study of co-firing pulverized coal and biomass inside a cement calciner. *Waste Manag. Res.* **2014**, *32*, 661–669. [\[CrossRef\]](#)
- Zeneli, M.; Nikolopoulos, A.; Nikolopoulos, N.; Grammelis, P.; Karellas, S.; Kakaras, E. Simulation of the reacting flow within a pilot scale calciner by means of a three phase TFM model. *Fuel Process. Technol.* **2017**, *162*, 105–125. [\[CrossRef\]](#)
- Wang, P.; Kao, H. Numerical Simulation of Sludge Combustion in TTF Precalciner. *J. Renew. Mater.* **2021**, *9*, 671–693. [\[CrossRef\]](#)
- Hu, Z.; Ma, X.; Chen, Y.; Liao, Y.; Wu, J.; Yu, Z.; Li, S.; Yin, L.; Xu, Q. Co-combustion of coal with printing and dyeing sludge: Numerical simulation of the process and related NO_x emissions. *Fuel* **2015**, *139*, 606–613. [\[CrossRef\]](#)
- ANSYS, Inc. *ANSYS Fluent Theory Guide*; ANSYS: Canonsburg, PA, USA, 2020.
- Kartushinsky, A.; Michaelides, E.E.; Hussainov, M.; Shcheglov, I.; Akhmadullin, I.; Hu, M.P. Eulerian–Eulerian RSTM-PDF Modeling of Turbulent Particulate Flow. *Mathematics* **2023**, *11*, 2647. [\[CrossRef\]](#)

22. Tong, C.; Chen, Z.; Chen, X.; Xie, Q. Research and Development of an Industrial Denitration-Used Burner with Multiple Ejectors via Computational Fluid Dynamics Analysis. *Mathematics* **2023**, *11*, 3476. [[CrossRef](#)]
23. Atashafrooz, M.; Nassab, S.G. Simulation of three-dimensional laminar forced convection flow of a radiating gas over an inclined backward-facing step in a duct under bleeding condition. *Proc. Inst. Mech. Eng. Part C J. Mech. Eng. Sci.* **2013**, *227*, 332–345. [[CrossRef](#)]
24. Atashafrooz, M.; Asadi, T.; Yan, W.M. Numerical study on forced convection in the exhaust problem using the spectral line-based weighted sum of gray gases model. *Int. J. Heat Mass Transf.* **2020**, *156*, 119837. [[CrossRef](#)]
25. Xu, S.-S.; Hao, W.; Liu, F.-H.; Yang, Y.-L.; Shi, Z.-M.; Ou, W.-J.; Xiao, Y.-Q. Simulation Study on the Optimum Bottom Cone Inlet Diameter of Coal Blends Combustion in the Precalciner. *Bull. Chin. Ceram. Soc.* **2016**, *35*, 2383–2388. [[CrossRef](#)]
26. Yin, C.; Yan, J. Oxy-fuel combustion of pulverized fuels: Combustion fundamentals and modeling. *Appl. Energy* **2016**, *162*, 742–762.
27. Zhang, J.; Zheng, S.; Chen, C.; Wang, X.; Tan, H. Kinetic model study on biomass pyrolysis and CFD application by using pseudo-Bio-CPD model. *Fuel* **2021**, *293*, 120266. [[CrossRef](#)]
28. Molintas, H.J.; Gupta, A.K. Combustion of Flat Shaped Char Particles With Oxygen. *J. Energy Resour. Technol.* **2022**, *144*, 022302. [[CrossRef](#)]
29. Pang, L.; Shao, Y.; Zhong, W.; Liu, H. Experimental study and modeling of oxy-char combustion in a pressurized fluidized bed combustor. *Chem. Eng. J.* **2023**, *418*, 129356. [[CrossRef](#)]
30. Nakhaei, M.; Wu, H.; Grévain, D.; Jensen, L.S.; Dam-Johansen, K. CPFD simulation of petcoke and SRF co-firing in a full-scale cement calciner. *Fuel Process. Technol.* **2019**, *196*, 106153. [[CrossRef](#)]
31. Liu, X.; Hao, W.; Wang, K.; Wang, Y.; Xu, G. Acquiring real kinetics of reactions in the inhibitory atmosphere containing product gases using micro fluidized bed. *AIChE J.* **2021**, *67*, e17325. [[CrossRef](#)]
32. Maya, J.C.; Chejne, F.; Gómez, C.A.; Bhatia, S.K. Effect of the CaO sintering on the calcination rate of CaCO₃ under atmospheres containing CO₂. *AIChE J.* **2018**, *64*, 1–55. [[CrossRef](#)]
33. Valverde, J.M.; Sanchez-Jimenez, P.E.; Perez-Maqueda, L.A. Limestone Calcination Nearby Equilibrium: Kinetics, CaO Crystal Structure, Sintering and Reactivity. *J. Phys. Chem. C* **2015**, *119*, 1623–1641. [[CrossRef](#)]
34. Ya, Y.; Zhang, D.; Chen, Z.; Jiang, Z.; Chen, X.; Deng, Y. Numerical modelling of multiphase FLOW and calcination process in an industrial calciner with fuel of heavy oil. *Powder Technol.* **2020**, *363*, 387–397. [[CrossRef](#)]
35. Hashimoto, N.; Watanabe, H.; Kurose, R.; Shirai, H. Effect of different fuel NO models on the prediction of NO formation/reduction characteristics in a pulverized coal combustion field. *Energy* **2017**, *118*, 47–59.
36. Zheng, Y.; Guo, Y.; Wang, J.; Luo, L.; Zhu, T. Ca Doping Effect on the Competition of NH₃-SCR and NH₃ Oxidation Reactions over Vanadium-Based Catalysts. *J. Phys. Chem. C* **2021**, *125*, 6128–6136. [[CrossRef](#)]
37. Xiao, X.; Luo, J.; Huang, H.; Xu, Z.; Fang, P. Study on the influencing factors of removal of NO_x from cement kiln flue gas by sewage sludge as a denitration agent. *Environ. Sci. Pollut. Res.* **2020**, *27*, 41342–41349. [[CrossRef](#)]

Disclaimer/Publisher's Note: The statements, opinions and data contained in all publications are solely those of the individual author(s) and contributor(s) and not of MDPI and/or the editor(s). MDPI and/or the editor(s) disclaim responsibility for any injury to people or property resulting from any ideas, methods, instructions or products referred to in the content.